CCFE
CULHAM CENTRE FOR FUSION ENERGY

UK Atomic Energy Authority

UKAEA-CCFE-PR(19)46

F. Riva, C. K. Tsui, J. A. Boedo, P. Ricci and the TCV Team

Shaping effects on scrape-off layer plasma turbulence: a rigorous validation of three-dimensional simulations against TCV measurements

Shaping effects on scrape-off layer plasma turbulence: a rigorous validation of three-dimensional simulations against TCV measurements

F. Riva, C. K. Tsui, J. A. Boedo, P. Ricci and the TCV Team

This is a preprint of a paper submitted for publication in
Physics of Plasmas

Shaping effects on scrape-off layer plasma turbulence: a rigorous validation of three-dimensional simulations against TCV measurements

F. Riva,[1,2,*] C. K. Tsui,[3,1] J. A. Boedo,[3] P. Ricci,[1] and the TCV Team[†]

[1] *École Polytechnique Fédérale de Lausanne (EPFL), Swiss Plasma Center (SPC), CH-1015 Lausanne, Switzerland*

[2] *United Kingdom Atomic Energy Authority, Culham Centre for Fusion Energy, Culham Science Centre, Abingdon, Oxon, OX14 3DB, UK*

[3] *Center for Energy Research (CER), University of California-San Diego (UCSD), La Jolla, California 92093, USA*

Abstract

The effect of plasma shaping on scrape-off layer (SOL) plasma turbulence is investigated through a rigorous validation exercise. Two- and three-dimensional simulations of the SOL plasma dynamics in three TCV limited discharges are carried out with the GBS code. These discharges realize an almost circular magnetic equilibrium, an elongated equilibrium, and an elongated equilibrium with negative triangularity. For the three plasma discharges, three simulations are performed, considering (i) a three-dimensional model with explicit dependence on elongation, triangularity, and inverse aspect ratio; (ii) a circular three-dimensional model in the infinite aspect ratio limit; and (iii) a two-dimensional model which assumes cold ions, infinite aspect ratio, and $k_{\parallel} = 0$. Ten validation observables common to simulations and experimental measurements from a reciprocating probe located at the TCV outer mid-plane are identified and the agreement between experiment and numerical results relative to each observable is evaluated. The composite metric introduced by P. Ricci *et al.* in [Phys. Plasmas **18**, 032109 (2011)] is then used to assess the overall agreement between simulations and experimental measurements. It is found that the shaping model implemented in GBS improves the description of SOL plasma turbulence taking into account the impact of elongation and triangularity and that, in general, three-dimensional simulations are in better agreement with experimental measurements than the numerical results obtained with the two-dimensional model.

*Electronic address: fabio.riva@ukaea.uk

†See author list of S. Coda *et al.*, Nucl. Fusion **57**, 102011 (2017)

I. INTRODUCTION

Simulation codes are playing an increasingly important role in optimizing and predicting the performance of present and future fusion devices. To limit potential errors arising from the use of the simulation results, there is an increasing motivation in the fusion community in developing and applying verification and validation (V&V) procedures [1–3]. Verification is "the process of determining that a model implementation accurately represents the developer's conceptual description of the model and the solution to the model", while validation is "the process of determining the degree to which a model is an accurate representation of the real world from the perspective of the intended uses of the model" [4]. In other words, verification and validation address the two questions "Does the code solve correctly the equations?" and "Does a model have the right equations?", respectively [5].

In the past few years, great effort was devoted to the development of V&V procedures for plasma turbulence simulations. A common approach used for verifying plasma simulation codes is code to code comparison (also known as code benchmark, see, e.g. Refs. [6–11]). More recently, a rigorous verification methodology based on the method of manufactured solutions was ported to the fusion community [12]. This procedure, generalized also to particle-in-cell codes [13], is now routinely used to assess the correct implementation of a model in a simulation code (see, e.g., Refs. [14–16]). Verification procedures are also used to quantify the numerical errors affecting simulation results (e.g., estimating the discretization error introduced by the use of a finite grid resolution). To this end, several methodologies have been ported to the fusion community in the recent past, including procedures based on convergence studies (see, e.g., Refs. [12, 13]).

Guidelines for performing a rigorous validation in the context of magnetic confinement fusion energy were laid down by the seminal works of Terry *et al.* [17] and Greenwald [18]. Main objectives of validation procedures include: the quantification of the degree of agreement of the code results, and therefore of the physics model, with experimental data to assess the maturity of our understanding of fusion-relevant systems; the comparison between different models to determine the most suitable one for describing a physical system; and the identification of parameter regimes where improvements to the current available models are needed. For carrying out a validation exercise, both Terry *et al.* [17] and Greenwald [18] works identify the following key steps: (i) the selection of a number (the more, the better) of physical

quantities common to simulation results and experimental measurements to be compared (typically referred as validation observables); (ii) the organization of the observables in a hierarchy based on the importance of the assumptions required for their evaluation, and therefore of their reliability; (iii) the evaluation of the agreement between experiments and simulations relative to each observable; and (iv) the definition of a composite metric, which combines the results for each observable and how stringent each observable is for comparison purposes, to quantify the overall agreement between simulations and experimental measurements. In performing these tasks, particular importance should be given to estimating and including in the metric the uncertainties affecting experimental measurements and numerical results. In this regard, it is clear that verification must precede validation.

An overview of best practices for the development of validation metrics and examples of their applications to fusion relevant problems are given in Refs. [19–22]. Among a number of examples, we consider here the validation methodology introduced by Ricci *et al.* in Refs. [23, 24], used for validating plasma turbulence simulations of the TORPEX device [25] against experimental measurements. This methodology can be summarized as follows. First, a number of independent and relevant physical quantities, common to the experiment and the simulations, should be identified and analyzed using the same technique. The values of the $j-$th observable at points $i = 1, ..., N_j$ (the index i can be used to discretize time and/or multidimensional spatial coordinates), as coming from experimental measurements or simulation results, are denoted as $e_{i,j}$ and $s_{i,j}$, respectively. Second, the measure of the distance d_j between experimental measurements and simulation results for the $j-$th observable is computed as

$$d_j = \sqrt{\frac{1}{N_j}\sum_{i=1}^{N_j}\frac{(e_{j,i}-s_{j,i})^2}{\Delta e_{j,i}^2+\Delta s_{j,i}^2}}, \tag{1}$$

where $\Delta e_{j,i}$ and $\Delta s_{j,i}$ are the uncertainties affecting $e_{i,j}$ and $s_{i,j}$, respectively. The level of agreement R_j between simulations and experiments with respect to the observable j is then given by

$$R_j = \frac{\tanh\left[(d_j - 1/d_j - d_0)/\lambda\right]+1}{2}, \tag{2}$$

such that $R_j = 0$ denotes perfect agreement and $R_j = 1$ complete disagreement. Here d_0 and λ are parameters used to set the threshold level for agreement and sharpness of transition from agreement to disagreement, respectively. In the following we consider $d_0 = 1$ and $\lambda = 0.5$, as suggested in Ref. [24]. This choice implies that $R_j \approx 0.5$ when the

discrepancy between the $j-$th experimental and numerical observables is comparable to their uncertainties. Finally, the overall agreement between simulations and experiments is measured by introducing a composite metric

$$\chi = \frac{\sum_j R_j H_j S_j}{\sum_j H_j S_j}, \tag{3}$$

which combines the level of agreement of each observable, R_j, with its weight, $H_j S_j$, which defines how stringent each observable is for comparison purposes, such that $\chi = 0$ means perfect agreement and $\chi = 1$ complete disagreement. Here H_j and S_j denote the weight of each observable j according to the number of assumptions made for its evaluation and the level of confidence characterizing its measurement, respectively. More precisely, H_j accounts approximately for the uncertainties related to model assumptions and/or to combinations of measurements, which are often needed to estimate the validation observables from the simulation results and the raw experimental data [26], and are generally very challenging to evaluate. In practice, the observables are organized into a hierarchy based on the number of assumptions required for their evaluation, h_j. Since the higher the hierarchy level of an observable is, the lower its importance in the comparison metric should be, H_j is a decreasing function of h_j. Following Ref. [23], we define $H_j = 1/h_j$. On the other hand, the quantity S_j is used to assess the precision of the measurement of the $j-$th observable and should be a decreasing function of the experimental and simulation uncertainties. Reference [23] proposes

$$S_j = \exp\left(-\frac{\sum_i \Delta e_{j,i} + \sum_i \Delta s_{j,i}}{\sum_i |e_{j,i}| + \sum_i |s_{j,i}|}\right). \tag{4}$$

Finally, Ref. [23] also introduces the index

$$Q = \sum_j H_j S_j, \tag{5}$$

used to assess the quality of the comparison itself. The idea is that a validation is more reliable with a large number of observables and if their weight $H_j S_j$ is large.

The goal of the present paper is twofold. First, we apply for the first time the validation methodology proposed in Ref. [23] to turbulence in tokamak scrape-off layer (SOL) conditions. More precisely, we simulate the turbulent SOL plasma dynamics in three limited discharges realized on the TCV tokamak [27] with different equilibrium magnetic shapes. We then use the composite metric χ to rigorously validate the numerical results against experimental measurements. Second, we assess the maturity of our understanding of plasma

shaping effects on SOL turbulence, thus validating the shaping model recently introduced in GBS [28]. As a matter of fact, there is experimental evidence that plasma shaping plays a strong role in regulating plasma turbulence, both in the core and in the SOL [29, 30]. In particular, plasma shaping might affect, e.g., the thermal loads on the first wall, one of the important issues the fusion program is facing today [31]. We note that, while the properties of SOL plasma turbulence in TCV have been investigated in the past both experimentally and numerically (see e.g., Refs. [32–36]), and the physics mechanisms behind the effect of plasma shaping on turbulence are discussed in Ref. [28], the present work focuses on the application of the rigorous validation methodology discussed above to investigate the impact of plasma shaping on SOL plasma dynamics.

For our simulations we use three different models, all based on the drift-reduced Braginskii equations [37, 38], considering (i) a three-dimensional model of SOL plasma turbulence in non-circular magnetic geometry, where we use the analytical equilibrium model discussed in Ref. [28] to introduce the dependence of the magnetic field on tokamak inverse aspect ratio, Shafranov's shift, elongation, and triangularity; (ii) a three-dimensional model in circular magnetic geometry and in the infinite aspect ratio limit; and (iii) a two-dimensional model in circular geometry and in the cold ion and $k_{\parallel} = 0$ limits. All these models are implemented in the GBS code [39, 40], which has been subject to a rigorous verification procedure [12, 40]. Three different simulations are carried out with each model, considering three TCV plasma discharges with (i) an almost circular magnetic equilibrium, (ii) plasma elongation $\kappa = 1.53$, and (iii) plasma elongation $\kappa = 1.57$ and triangularity $\delta = -0.19$. The simulation results are then compared with TCV experimental measurements obtained with a horizontal reciprocating probe located at the tokamak outer mid-plane [41]. For this purpose, ten observables are considered. The composite metric χ is finally used to quantify the level of agreement between the simulations and the experiments for the three models and assess the maturity of our understanding of plasma shaping effects on SOL turbulence.

The present paper is structured as follows. After this introduction, in Sec. II we discuss the three models considered for this study. Then, in Sec. III we illustrate the TCV experimental setup, the probes used to collect the experimental measurements, and the simulations we carried out. In Sec. IV we present the validation observables considered for our analysis and the agreement between experimental measurements and numerical results with respect to every single observable. Finally, the validation metric χ and the quality factor Q are

computed for the three models and discussed in Sec. V. We note that the present paper is an extension of the work illustrated in Chapter 7 of Ref. [42].

II. SIMULATION MODELS

Since the tokamak SOL is characterized by rather low temperatures and relatively high collisionality, a fluid model based on the Braginskii equations [37] is typically employed to describe the plasma dynamics in this region. Moreover, because SOL turbulence occurs on timescales much slower than the gyromotion and it is usually characterized by spatial variations that occur on scale lengths longer than the ion gyroradius, the drift approximation is often adopted. The set of equations to describe plasmas in such conditions, known as drift-reduced Braginskii equations [38], was implemented in the GBS code to simulate plasma turbulence at the tokamak periphery [39, 40].

GBS is a three-dimensional flux-driven, two-fluid, turbulence code that solves the drift-reduced Braginskii equations numerically by using finite differences for the spatial discretization and a standard fourth-order Runge–Kutta method for the time advance. Increasingly complex magnetic configurations were considered in developing GBS. Initially, the code was used to simulate linear devices such as LAPD [43] and simple magnetized toroidal devices such as TORPEX [44]. GBS was then extended to limited SOL tokamak circular geometries [39]. More recently, the capabilities of simulating non-circular geometries and diverted configurations were also introduced [28, 45].

For our study, we consider the GBS model in the electrostatic limit and we employ the Boussinesq approximation to simplify the vorticity equation (the validity of this assumption in modelling the SOL plasma dynamics is discussed in Refs. [46–49]). The resulting system

of equations writes

$$\frac{\partial n}{\partial t} = -\frac{1}{B}\{\phi, n\} + \frac{2}{eB}\left[C\left(p_e\right) - enC\left(\phi\right)\right] - \nabla\cdot\left(nv_{\parallel e}\mathbf{b}\right) + \mathcal{D}_n(n) + S_n, \tag{6}$$

$$\frac{\partial \omega}{\partial t} = -\frac{1}{B}\{\phi, \omega\} + \frac{2B}{m_i n}C\left(p_e + p_i\right) - v_{\parallel i}\nabla_\parallel\omega + \frac{B^2}{m_i n}\nabla\cdot\left(j_\parallel\mathbf{b}\right) + \frac{B}{3m_i n}C\left(G_i\right) + \mathcal{D}_\omega(\omega), \tag{7}$$

$$\frac{\partial v_{\parallel e}}{\partial t} = -\frac{1}{B}\left\{\phi, v_{\parallel e}\right\} + \frac{1}{m_e}\left[e\nabla_\parallel\phi - \frac{\nabla_\parallel p_e}{n} - 0.71\nabla_\parallel T_e + \frac{ej_\parallel}{\sigma_\parallel} - \frac{2}{3n}\nabla_\parallel G_e\right] - v_{\parallel e}\nabla_\parallel v_{\parallel e} + \mathcal{D}_{v_{\parallel e}}(v_{\parallel e}), \tag{8}$$

$$\frac{\partial v_{\parallel i}}{\partial t} = -\frac{1}{B}\left\{\phi, v_{\parallel i}\right\} - v_{\parallel i}\nabla_\parallel v_{\parallel i} - \frac{1}{m_i n}\nabla_\parallel\left(p_e + p_i\right) - \frac{2}{3m_i n}\nabla_\parallel G_i + \mathcal{D}_{v_{\parallel i}}(v_{\parallel i}), \tag{9}$$

$$\frac{\partial T_e}{\partial t} = -\frac{1}{B}\{\phi, T_e\} + \frac{4T_e}{3eB}\left[\frac{C\left(p_e\right)}{n} + \frac{5}{2}C\left(T_e\right) - eC\left(\phi\right)\right] - v_{\parallel e}\nabla_\parallel T_e + S_{T_e} + \frac{2T_e}{3}\left[0.71\frac{\nabla\cdot\left(j_\parallel\mathbf{b}\right)}{en} - \nabla\cdot\left(v_{\parallel e}\mathbf{b}\right)\right] + \nabla_\parallel\left(\chi_{\parallel e}\nabla_\parallel T_e\right) + \mathcal{D}_{T_e}(T_e), \tag{10}$$

$$\frac{\partial T_i}{\partial t} = -\frac{1}{B}\{\phi, T_i\} + \frac{4T_i}{3eB}\left[\frac{C(p_e)}{n} - \frac{5}{2}C(T_i) - eC(\phi)\right] - v_{\parallel i}\nabla_\parallel T_i + S_{T_i} + \frac{2T_i}{3}\left[\frac{\nabla\cdot\left(j_\parallel\mathbf{b}\right)}{en} - \nabla\cdot\left(v_{\parallel i}\mathbf{b}\right)\right] + \nabla_\parallel\left(\chi_{\parallel i}\nabla_\parallel T_i\right) + \mathcal{D}_{T_i}(T_i), \tag{11}$$

where $\omega = \nabla_\perp^2\phi + \nabla_\perp^2 T_i/e$ is the plasma vorticity, $j_\parallel = en(v_{\parallel i} - v_{\parallel e})$ the parallel current, $p_e = nT_e$ and $p_i = nT_i$ the electron and ion plasma pressures, $\chi_{\parallel e}$ and $\chi_{\parallel i}$ the parallel electron and ion thermal conductivities, B the norm of the magnetic field, $\mathbf{b}$ the unitary vector oriented in the direction of $\mathbf{B}$, and $\sigma_\parallel = 1.96e^2 n\tau_e/m_e$ the Spitzer conductivity, with τ_e the electron collision time. The density and temperature sources, S_n, S_{T_e}, S_{T_i}, are used to mimick the particles and heat outflow from the core. The gyro-viscous contributions are included in the model through the $G_i = -\eta_{0i}[2\nabla_\parallel v_{\parallel i} + C\left(\phi\right)/B + C\left(p_i\right)/(enB)]$ and $G_e = -\eta_{0e}[2\nabla_\parallel v_{\parallel e} + C\left(\phi\right)/B - C\left(p_e\right)/(enB)]$ terms, with η_i and η_e the gyro-viscous coefficients [37]. Moreover, small perpendicular diffusion terms of the form $\mathcal{D}_A(A) = D_A\nabla_\perp^2 A$, with $A = n, \omega, \phi, v_{\parallel i}, v_{\parallel e}, T_e, T_i$, are introduced for numerical stability reasons. Here the Poisson brackets are defined as $\{\phi, A\} = \mathbf{b}\cdot(\nabla\phi\times\nabla A)$, the curvature operator as $C\left(A\right) = B/2\left[\nabla\times(\mathbf{b}/B)\right]\cdot\nabla A$, the perpendicular Laplacian as $\nabla_\perp^2 A = -\nabla\cdot[\mathbf{b}\times(\mathbf{b}\times\nabla A)]$, and the parallel gradient as $\nabla_\parallel A = \mathbf{b}\cdot\nabla A$. Equations (6)-(11) are completed by a set of boundary conditions describing the plasma dynamics at the magnetic pre-sheath entrance, as detailed in Refs. [50, 51].

The dependence on the magnetic field geometry enters in the model through the norm of the magnetic field B, the direction of the unit vector $\mathbf{b}$, and the differential operators $\{\phi, A\}$, $C(A)$, $\nabla_\parallel(A)$, and $\nabla^2_\perp(A)$. A model for expressing these quantities in limited, non-circular magnetic geometries has been recently introduced in GBS [28]. This model can be used to investigate the effect of plasma elongation, κ, and plasma triangularity, δ, on SOL turbulence. The magnetic field depends also on the tokamak major radius, R_0, the inverse aspect ratio, $\epsilon = a/R_0$ (a is the tokamak minor radius), the safety factor at the magnetic axis, q_0, and at the last closed flux surface (LCFS), q_a.

In order to validate the shaping model in Ref. [28] against experimental measurements and gain a deeper insight on the SOL turbulence properties, in the following we consider: (i) Eqs. (6)-(11) with the magnetic equilibrium given in Ref. [28], referred to as "Shaping model" in the following, (ii) Eqs. (6)-(11) with a circular equilibrium in the infinite aspect ratio limit, $\epsilon = 0$, and with negligible Shafranov's shift (the model is described in Ref. [51]), referred to as "Circular model"; and (iii) Eqs. (6)-(11) in the cold ion and $\epsilon = 0$ limits, reduced to a two-dimensional model assuming $k_\parallel = 0$, referred to as "2D model". More precisely, the "2D model" equations write

$$\frac{\partial n}{\partial t} = -\frac{1}{B_0}\{\phi, n\} + \frac{2}{eRB_0}\left(\frac{\partial p_e}{\partial y} - en\frac{\partial \phi}{\partial y}\right) - \frac{\sigma n c_s}{R}\exp\left(\Lambda - \frac{e\phi}{T_e}\right) + \mathcal{D}_n(n) + S_n, \tag{12}$$

$$\frac{\partial \omega}{\partial t} = -\frac{1}{B_0}\{\phi, \omega\} + \frac{2B_0}{m_i R n}\frac{\partial p_e}{\partial y} + \frac{\sigma c_s \omega_{ci}^2 m_i}{eR}\left[1 - \exp\left(\Lambda - \frac{e\phi}{T_e}\right)\right] + \mathcal{D}_\omega(\omega), \tag{13}$$

$$\begin{aligned}\frac{\partial T_e}{\partial t} = &-\frac{1}{B_0}\{\phi, T_e\} + \frac{4T_e}{3eRB_0}\left(\frac{1}{n}\frac{\partial p_e}{\partial y} + \frac{5}{2}\frac{\partial T_e}{\partial y} - e\frac{\partial \phi}{\partial y}\right) \\ &- \frac{2\sigma T_e c_s}{3R}\left[1.71\exp\left(\Lambda - \frac{e\phi}{T_e}\right) - 0.71\right] + \mathcal{D}_{T_e}(T_e) + S_{T_e},\end{aligned} \tag{14}$$

where $c_s = \sqrt{T_e/m_i}$ is the sound speed, B_0 the norm of the magnetic field at the outer mid-plane of the LCFS, $\omega_{ci} = eB_0/m_i$ the ion cyclotron frequency, $y = a\theta$ the poloidal coordinate, $\Lambda \approx 3.2$ for deuterium plasmas, and $\sigma = R/L_c \approx 1/(2\pi q_a)$, with θ the poloidal angle and $L_c \approx 2\pi qR$ the connection length. Note that the "2D model" equations correspond to Eqs. (B6)-(B8) in Ref. [24].

III. EXPERIMENTAL AND SIMULATION SETUPS

The TCV experiment is a tokamak with major and minor radii $R_0 = 0.88\,\mathrm{m}$ and $a = 0.25\,\mathrm{m}$, respectively [27]. By being equipped with sixteen independent shaping and positioning coils, TCV has unique capabilitities of exploring a wide range of magnetic geometries, including negative triangularities, second-order X points, and more exotic plasma shapes [52]. For this reason, TCV is an ideal test bed for validating the plasma shaping model introduced in Ref. [28] against experimental measurements.

In the following we consider the three TCV inner-wall limited deuterium plasma discharges #54147, #55391, and #55394. The experimental parameters measured for the three discharges are summarized in Table I and the poloidal cross sections of their magnetic surfaces are shown in Fig. 1. The plasma has an almost circular magnetic equilibrium in the discharge #55391, an elongated equilibrium in the discharge #55394, and an elongated equilibrium with negative triangularity in the discharge #54147. The thick blue continuous lines, representing the LIUQE [53] reconstruction of the LCFS, are best fitted by the model discussed in Ref. [28] (red dashed lines), showing a good agreement of the fitting with the magnetic reconstruction. We note that the three discharges have similar safety factors, q_a, densities, n_a, and temperatures, $T_{e,a}$, at the LCFS. This allows us to decouple the influence of plasma shaping on the SOL dynamics from other effects [28].

TABLE I: Tokamak major radius, inverse aspect ratio, edge safety factor, plasma elongation and triangularity, toroidal magnetic field on axis, plasma density and electron temperature at the LCFS, and sound Larmor radius, for the three TCV plasma discharges #54147, #55391, and #55394. The magnetic equilibrium parameters are obtained by best fitting the profiles shown in Fig. 1 with the shaping model in Ref [28].

Discharge	R_0 [m]	ϵ	q_a	κ	δ	B_0 [T]	n_a [$10^{18}\,\mathrm{m}^{-3}$]	$T_{e,a}$ [eV]	ρ_{s0} [mm]
#54147	0.875	0.34	3.3	1.57	-0.19	1.44	6 ± 2	37 ± 15	0.61
#55391	0.870	0.30	3.4	1.07	0.00	1.45	4 ± 1	36 ± 16	0.60
#55394	0.865	0.30	3.2	1.53	0.00	1.46	5 ± 1	41 ± 14	0.63

The experimental measurements discussed in the following are obtained with a horizontal reciprocating probe located at the tokamak outer mid-plane. This diagnostic provides high

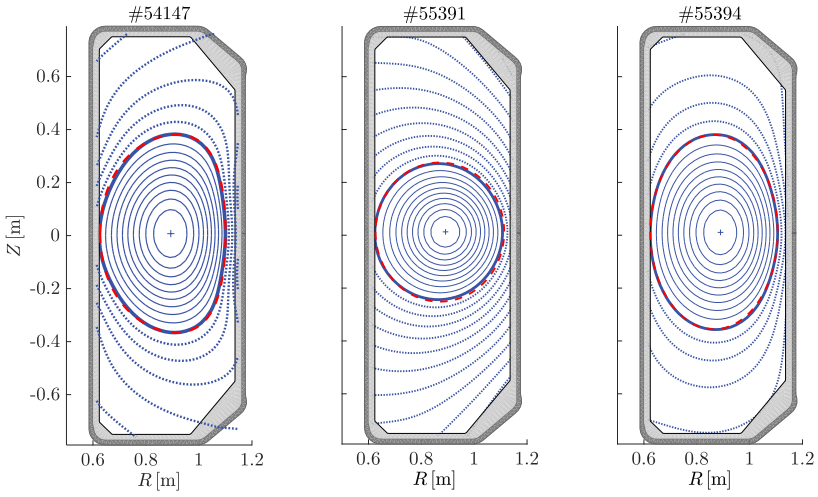

FIG. 1: Poloidal cross sections of the magnetic surfaces for the three TCV plasma discharges #54147 (left panel), #55391 (middle panel), and #55394 (right panel). The blue lines indicate the LIUQE reconstruction, with thin continuous lines denoting the core flux surfaces, thick continuous lines denoting the LCFS, and dashed lines denoting the open field line region. The red dashed lines represent the reconstruction of the LCFS with the shaping model discussed in Ref. [28].

spatial resolution measurements of time-averaged and fluctuating physical quantities. It is equipped with a probe head having ten electrostatic pins (two are used as a swept double probe and provide measurements of I_{sat}, n, and T_e, one is used to obtain direct measurements of I_{sat}, five are used as floating Langmuir probes to measure V_{fl}, and the last two are used to measure the poloidal Mach number). Taking the difference of two of the V_{fl} pins, it is possible to estimate the poloidal electric field E_θ. Radial profiles related to the measured quantities are obtained by sampling the measured time traces in intervals of 1 ms. For a more detailed description of the reciprocating probe we refer to Refs. [41, 54].

To assess the reliability of the models illustrated in Sec. II, we compare nonlinear GBS simulations based on the three TCV plasma discharges discussed above with experimental TCV measurements. For each TCV plasma discharge we perform three simulations, one with the "Shaping model", one with the "Circular model", and one with the "2D model". For our simulations we consider perpendicular diffusion coefficients $D_A \approx 0.1\,\mathrm{m^2 s^{-1}}$, with A indicating all evolved fields. The particle and temperature sources are assumed poloidally and toroidally constant, with radial dependence $S_n(x), S_{T_e}(x), S_{T_i}(x) \propto \exp\left[-(x-a+\sigma)^2/\sigma^2\right]$, where $\sigma = 2.5\rho_{s0}$ and ρ_{s0} is the sound Larmor radius reported in Table I and x is the radial

coordinate, and we adjust the amplitude of the sources such that the simulated plasma densities and temperatures agree within uncertainties with the experimental measurements at the LCFS. We use $q_0 = 1$ for the "Shaping model" simulations. The radial domain extends from the inner radius $x_i = a-30\rho_{s0}$ to the outer radius $x_o = a+70\rho_{s0}$. Ad hoc boundary conditions are applied at x_i and x_o, with Neumann's boundary conditions used for n, $v_{\parallel e}$, $v_{\parallel i}$, T_e, and T_i, and Dirichlet's boundary conditions for ω and ϕ. To mitigate the impact of these boundary conditions on the simulation results, the two regions extending from $x = x_i$ to $x = a$, and from $x = a + 2.5\,\mathrm{cm}$ to $x = x_o$ are considered as buffers and are not included in the analysis of the results. Moreover, for the three-dimensional simulations we consider an ion to electron temperature ratio $T_e/T_i = 1$ at the LCFS, as indicated by typical charge exchange measurements in TCV. We note that, since the three-dimensional simulations require three rather large numerical grids $(N_x, N_y, N_z) = (128, 1280, 196), (128, 1280, 188), (128, 1280, 200)$, with z the toroidal coordinate and N_x, N_y, and N_z the number of grid points in x, y, and z, respectively, heavy electrons, $m_i/m_e = 800$, and a reduced parallel electron thermal conductivity, $\chi_{\parallel e} \approx 5 \cdot 10^5\,\mathrm{m}^2 s^{-1}$, are used to considerably decrease the computational cost. For the two-dimensional simulations we use the numerical grid $(N_x, N_y) = (128, 512)$, with the poloidal direction extending over a distance $2\pi a/q$. Finally, we also note that, to investigate the effect of the uncertainty of input parameters, we performed an additional "Shaping model" simulation of the plasma discharge #54147 using $\sigma_\parallel$ ten times smaller than its estimated Spitzer value.

IV. VALIDATION OBSERVABLES

To validate the GBS simulations discussed in Sec. III against TCV experimental measurements, we consider the following observables: the time-averaged plasma density, electron temperature, and ion saturation gradient lengths, L_n, L_{T_e}, and $L_{j_{sat}}$; the root mean square (RMS) of j_{sat} fluctuations normalized to the j_{sat} time-averaged profile, $\delta j_{sat}^{RMS}/\bar{j}_{sat}$, the RMS profiles of floating potential and of electric field fluctuations, δV_{fl}^{RMS} and δE_θ^{RMS}; the δj_{sat} and δV_{fl} probability distribution functions (PDF); and the j_{sat} and V_{fl} power spectral-slopes, $\alpha_{j_{sat}}$ and $\alpha_{V_{fl}}$. Concerning the experimental measurements, we note that n and j_{sat} are obtained both from direct I_{sat} and double probe measurements, T_e is obtained using the double probe only, V_{fl} is obtained from one of the floating Langmuir probes, while E_θ is obtained

by comparing the measurements of two poloidally separated floating potential Langmuir probes (i.e., we assume no difference in plasma temperature between the two electrodes). All measurements are taken twice, with the probe entering and exiting the plasma, providing at each radial position four independent measurements of n and j_{sat} and two independent measurements of all other plasma quantities.

Concerning the numerical results, these are obtained with simulations in turbulent quasi-steady state on time intervals of approximately $200\,\mu$s. We note that n and T_e are direct output of GBS, E_θ is obtained by combining GBS time-traces of ϕ at two different poloidal locations, and we assume $j_{sat} \propto n\sqrt{T_e + 2T_i}$, consistently with Ref. [55], and $V_{fl} = \phi - [\Lambda - \log(1 + T_i/T_e)/2]T_e$. However, since the "2D model" does not evolve the ion temperature, we assume $T_i = T_e$ in evaluating j_{sat} and V_{fl} from the two-dimensional results. In the following subsections, we discuss in more detail the evaluation of all observables, focusing on their uncertainties, their hierarchy level, h, their level of agreement, R, and their accuracy parameter, S.

A. Gradient scale lengths

Some of the main uncertainties affecting the design and operation of future fusion devices are closely related to our ability of predicting the characteristic gradient lengths of SOL equilibrium profiles. Therefore, three of the validation observables considered in our study are the characteristic gradient lengths L_n, L_{T_e}, and $L_{j_{sat}}$. For the plasma density, this is defined as $L_n = -\bar{n}/\partial_x\bar{n}$, where $\bar{n}(x)$ is the time-averaged plasma density radial profile. Similar definitions apply to L_{T_e} and $L_{j_{sat}}$.

In TCV, the time-averaged radial profiles are evaluated by considering time-average windows of 1 ms. The value of the characteristic gradient lengths are then obtained by best-fitting the radial profiles with an exponential. More specifically, taking the plasma density as an example, we best-fit each of the four indipendent measurements assuming $\bar{n}(x) \propto \exp(-x/L_n)$. We then compute L_n as the average of the four resulting values. We note that, while decay lengths in the SOL are known to be non-exponential [54, 56, 57], in our analysis we best-fit the radial profiles with a single exponential for simplicity. The uncertainty arising from such simplification should therefore be taken into account in Δe_{L_n}, as discussed in the following. We consider two different sources of uncertainty affecting these measurements. The first

TABLE II: Plasma density, electron temperature and ion saturation current gradient scale lengths and corresponding total uncertainties.

	#54147			#55391			#55394		
	L_n [cm]	L_{T_e} [cm]	$L_{j_{sat}}$ [cm]	L_n [cm]	L_{T_e} [cm]	$L_{j_{sat}}$ [cm]	L_n [cm]	L_{T_e} [cm]	$L_{j_{sat}}$ [cm]
Experimental	2.3±0.6	6.3±12.6	1.8±0.6	5.3±2.4	6.4±6.1	3.4±1.1	2.2±0.8	3.4±2.5	1.7±0.5
"Shaping model"	2.0±0.1	3.1±0.2	1.6±0.1	2.4±0.1	3.7±0.1	1.8±0.1	2.2±0.1	3.1±0.1	1.7±0.1
"Circular model"	3.9±0.1	5.2±0.2	2.9±0.1	3.7±0.1	4.8±0.1	2.7±0.1	3.8±0.2	5.3±0.3	2.8±0.1
"2D model"	13.8±0.4	21.7±0.6	10.4±0.3	14.2±0.5	22.2±0.6	10.7±0.3	14.0±0.5	22.0±0.7	10.6±0.4

source is due to the best-fitting of the radial profiles with an exponential, referred to as $\Delta e^{fit}_{L_n}$, while the second source is due to the uncertainties on the measurements of $\bar{n}_k(x)$, referred in the following as $\Delta e^{meas}_{L_n}$. For our validation, we take $\Delta e^{fit}_{L_n}$ as given by the 95% confidence interval of the exponential fit of $\bar{n}(x)$ and we define $\Delta e^{meas}_{L_n}$ as the standard deviation of the four individual measurements. Finally, we obtain the total experimental uncertainty on L_n as $\Delta e^2_{L_n} = (\Delta e^{fit}_{L_n})^2 + (\Delta e^{meas}_{L_n})^2$ if $\Delta e^{meas}_{L_n} > \Delta e^{fit}_{L_n}$, while we consider $\Delta e_{L_n} = \Delta e^{fit}_{L_n}$ otherwise. The same procedure is used for L_{T_e}, $L_{j_{sat}}$, and the corresponding uncertainties. The resulting experimental gradient scale lengths and the corresponding total uncertainties are reported in Table. II. We see that elongation and negative triangularity reduce the experimental gradient scale lengths, consistently with the results reported in Ref. [28].

Concerning the numerical results, the time-averaged profiles for the three-dimensional simulations are obtained by performing the toroidal- and time-averages of n, T_e, and I_{sat} at the outer equatorial mid-plane. Similarly, for two-dimensional simulations the poloidal- and time-averages profiles are considered. The characteristic gradient lengths and Δs^{fit}_L, with $L = L_n, L_{T_e}, L_{j_{sat}}$, are then obtained by best-fitting the time-averaged profiles with an exponential, as discussed for the experimental measurements. Since the simulation results are evaluated on time intervals shorter than those considered for the experimental measurements, among the simulation uncertainties we also account for statistical fluctuations, Δs^{stat}_L. The values of Δs^{stat}_L are obtained by averaging the simulation results on two sub-intervals of approximately $100\,\mu$s, computing L for each sub-interval, and evaluating Δs^{stat}_L as the standard deviation of the two resulting gradient scale lengths. Finally, we use $\Delta s^2_L = (\Delta s^{fit}_L)^2 + (\Delta s^{stat}_L)^2$ if $\Delta s^{stat}_L > \Delta s^{fit}_L$, while we consider $\Delta s_L = \Delta s^{fit}_L$ otherwise. We

TABLE III: Level of agreement between simulations and experiments with respect to gradient scale lengths.

	#54147			#55391			#55394		
	R_{L_n}	$R_{L_{T_e}}$	$R_{L_{j_{sat}}}$	R_{L_n}	$R_{L_{T_e}}$	$R_{L_{j_{sat}}}$	R_{L_n}	$R_{L_{T_e}}$	$R_{L_{j_{sat}}}$
"Shaping model"	0.00	0.00	0.00	0.09	0.00	0.31	0.00	0.00	0.00
"Circular model"	1.00	0.00	0.82	0.00	0.00	0.00	0.90	0.00	0.98
"2D model"	1.00	0.09	1.00	1.00	0.99	1.00	1.00	1.00	1.00

note that here we neglect numerical uncertainties and uncertainties due to input parameters on gradient scale lengths. The numerical uncertainties introduced by the time and space discretization are neglected because they are rather small, of the order of the grid spacing, for typical GBS simulations [12]. The propagation of uncertainties on input parameters through model equations are neglected because they are typically smaller than Δs_L^{fit} (for the three-dimensional simulations this was assessed by performing a sensitivity scan in plasma resistivity, as discussed at the beginning of this section, while for the two-dimensional simulations this is discussed in detail in Ref. [58]). The resulting gradient scale lengths and the corresponding total uncertainties are reported in Table. II. We see that elongation and negative triangularity decrease the gradient scale lengths obtained with the "Shaping model". This is in qualitative agreement with experimental measurements. Moreover, by comparing the three-dimensional simulation results for the plasma discharge #55391, we observe that Shafranov's shift and ϵ effects reduce the SOL width, consistently with Ref. [28]. For the two-dimensional simulations, we note that the "2D model" over-predicts the gradient scale lengths in all cases, both if compared to experimental measurements and to three-dimensional simulation results. To carry out a more quantitative comparison, in Table III we present the level of agreement between simulations and experiments with respect to the gradient scale lengths. Concerning the non-circular TCV discharges, we see that the "Shaping model" is generally in better agreement with the experimental measurements than the "Circular model". On the other hand, the "Circular model" is in slightly better agreement than the "Shaping model" with the experimental measurements for the #55391 plasma discharge. This seems to suggest that Shafranov's shift and ϵ effects introduced in the "Shaping

TABLE IV: Accuracy parameters for the gradient scale lengths.

	#54147			#55391			#55394		
	S_{L_n}	$S_{L_{T_e}}$	$S_{L_{j_{sat}}}$	S_{L_n}	$S_{L_{T_e}}$	$S_{L_{j_{sat}}}$	S_{L_n}	$S_{L_{T_e}}$	$S_{L_{j_{sat}}}$
"Shaping model"	0.85	0.26	0.83	0.73	0.54	0.81	0.83	0.68	0.86
"Circular model"	0.90	0.33	0.88	0.77	0.57	0.83	0.86	0.72	0.87
"2D model"	0.94	0.62	0.93	0.87	0.79	0.90	0.93	0.88	0.94

model" over-stabilize the SOL plasma turbulence. In general, two-dimensional simulations completely disagree with experimental measurements.

In Table IV we report the accuracy parameters. In most cases, uncertainties on gradient scale lengths are rather small and S_L is typically larger than 0.7. On the other hand, for the plasma discharges #54147 and #55391, large experimental uncertainties on measuring $\bar{T}_e$ (reported in Table II) significantly reduce $S_{L_{T_e}}$.

Finally, as discussed in Ref. [26], $h_L = 2$ for L_n, L_{T_e}, and $L_{j_{sat}}$. Indeed, the only assumption made to obtain the gradient scale lengths for the $\bar{n}$, $\bar{T}_e$, and $\bar{j}_{sat}$ profiles is that the time-averaged radial profiles are exponentially decaying and the uncertainties introduced by this assumption are taken into account in Δe_L and Δs_L.

B. Fluctuation amplitudes

Important quantities used to characterize plasma turbulence in the tokamak SOL are related to the amplitude of the fluctuations. Therefore, in our validation we also consider the RMS j_{sat} fluctuations normalized to the j_{sat} background, $\delta j_{sat}^{RMS}/\bar{j}_{sat}$, the RMS floating potential fluctuations, δV_{fl}^{RMS}, and the RMS poloidal electric field fluctuations, δE_θ^{RMS}.

Concerning the uncertainties affecting the experimental measurements, taking $\delta j_{sat}^{RMS}/\bar{j}_{sat}$ as an example, we compute $(\delta j_{sat}^{RMS}/\bar{j}_{sat})$ for each independent measurements of j_{sat}. We then evaluate $\Delta e_{\delta j_{sat}^{RMS}/\bar{j}_{sat}}$ as the standard deviation of the four resulting values. The same procedure is used to evaluate $\Delta e_{\delta V_{fl}^{RMS}}$ and $\Delta e_{\delta E_\theta^{RMS}}$. We neglect other sources of uncertainty.

Concerning the numerical results, we consider three sources of uncertainty. The first one

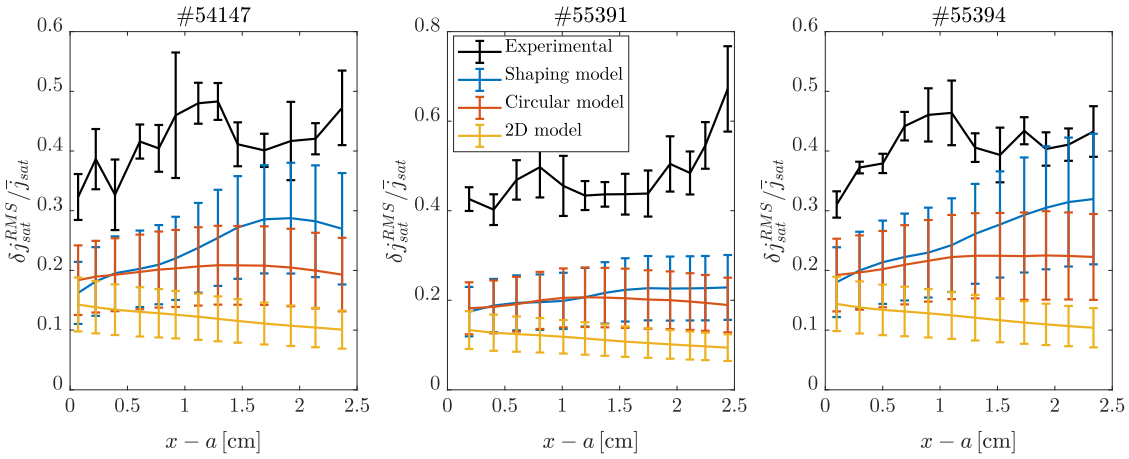

FIG. 2: Radial profiles of RMS j_{sat} fluctuations normalized to the j_{sat} background for the three plasma discharges #54147, #55391, and #55394.

($\Delta s_{\delta A}^{num}$, with $\delta A = \delta j_{sat}^{RMS}, \delta V_{fl}^{RMS}, \delta E_{\theta}^{RMS}$) is introduced by discretizing the model equations in time and space, and it is evaluated by applying the solution verification procedure described in Ref. [12] to typical GBS simulations. We find that, for a resolution similar to the one used in this study, $\Delta s_{\delta j_{sat}^{RMS}/\bar{j}_{sat}}^{num} \approx 0.3\delta j_{sat}^{RMS}/\bar{j}_{sat}$, $\Delta s_{\delta E_{\theta}^{RMS}}^{num} \approx 0.1\delta E_{\theta}^{RMS}$, and $\Delta s_{\delta V_{fl}^{RMS}}^{num} \approx 0.2\delta V_{fl}^{RMS}$. The second source of uncertainty ($\Delta s_{\delta A}^{inp}$) is related to the propagation of uncertainties on input parameters. Since a tenfold increase of the plasma resistivity in typical GBS simulations generally leads to a 10% increase of SOL fluctuations, we assume $\Delta s_{\delta A}^{inp} = 0.1\delta A$. The last source of uncertainty ($\Delta s_{\delta A}^{stat}$) is due to statistical fluctuations. This is evaluated by splitting the synthetic time traces into two sub-intervals, computing $\delta j_{sat}^{RMS}/\bar{j}_{sat}$, δV_{fl}^{RMS}, and δE_{θ}^{RMS} on each sub-interval, and evaluating $\Delta s_{\delta A}^{stat}$ as the standard deviation of the resulting values. The total uncertainties are then computed as $\Delta s_{\delta A}^2 = (\Delta s_{\delta A}^{num})^2 + (\Delta s_{\delta A}^{inp})^2 + (\Delta s_{\delta A}^{stat})^2$.

The radial profiles of $\delta j_{sat}^{RMS}/\bar{j}_{sat}$, δV_{fl}^{RMS}, and δE_{θ}^{RMS} and the corresponding total uncertainties are displayed in Figs. 2, 3, and 4, respectively. We see that, in general, GBS simulations underestimate j_{sat} fluctuations. This is consistent with previous observations, as discussed in Ref. [59]. On the other hand, E_{θ} fluctuations are overestimated by all three models. In Fig. 3 we also observe that better agreement is found for δV_{fl}^{RMS}, in particular for the "2D model".

To investigate more quantitatively the agreement between experimental measurements and simulation results with respect to the fluctuation amplitudes, in Tables V and VI we present

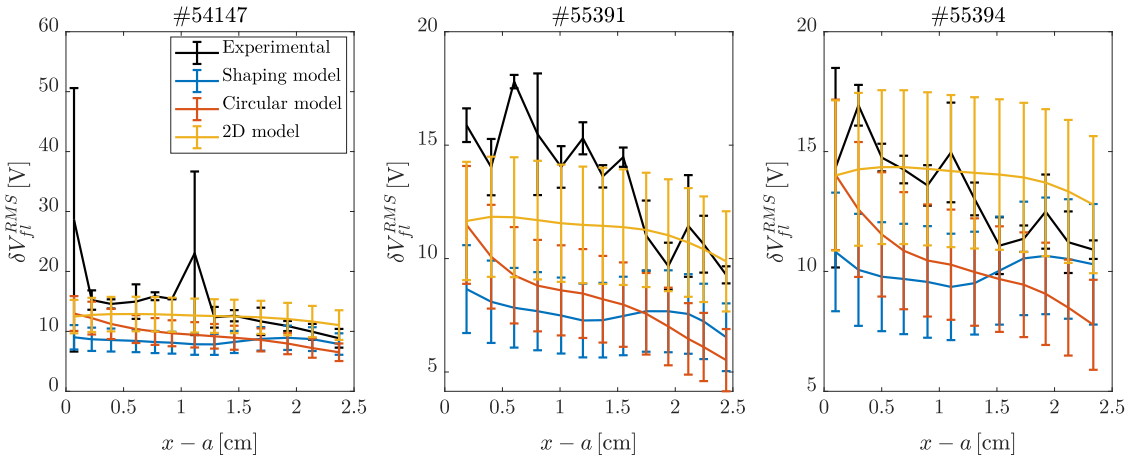

FIG. 3: Radial profiles of RMS V_{fl} fluctuations for the three plasma discharges #54147, #55391, and #55394.

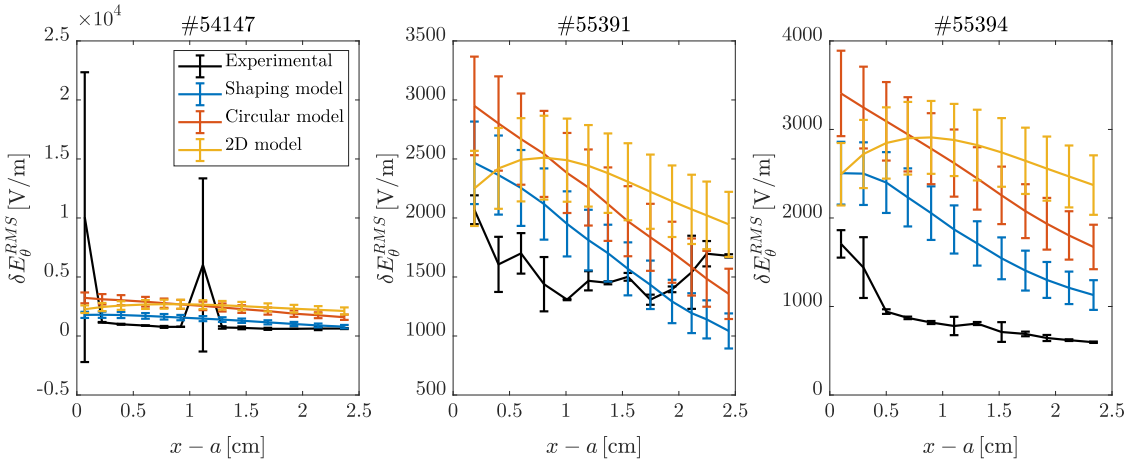

FIG. 4: Radial profiles of RMS E_θ fluctuations for the three plasma discharges #54147, #55391, and #55394.

TABLE V: Level of agreement between simulations and experiments with respect to RMS fluctuations.

	#54147			#55391			#55394		
	$R_{\delta j_{sat}^{RMS}/\bar{j}_{sat}}$	$R_{\delta V_{fl}^{RMS}}$	$R_{\delta E_\theta^{RMS}}$	$R_{\delta j_{sat}^{RMS}/\bar{j}_{sat}}$	$R_{\delta V_{fl}^{RMS}}$	$R_{\delta E_\theta^{RMS}}$	$R_{\delta j_{sat}^{RMS}/\bar{j}_{sat}}$	$R_{\delta V_{fl}^{RMS}}$	$R_{\delta E_\theta^{RMS}}$
"Shaping model"	0.94	0.95	0.99	1.00	1.00	0.81	0.85	0.29	1.00
"Circular model"	1.00	0.34	1.00	1.00	0.99	0.89	0.99	0.08	1.00
"2D model"	1.00	0.00	1.00	1.00	0.03	0.96	1.00	0.00	1.00

TABLE VI: Accuracy parameters for the RMS fluctuations.

	#54147			#55391			#55394		
	$S_{\delta j_{sat}^{RMS}/\bar{j}_{sat}}$	$S_{\delta V_{fl}^{RMS}}$	$S_{\delta E_\theta^{RMS}}$	$S_{\delta j_{sat}^{RMS}/\bar{j}_{sat}}$	$S_{\delta V_{fl}^{RMS}}$	$S_{\delta E_\theta^{RMS}}$	$S_{\delta j_{sat}^{RMS}/\bar{j}_{sat}}$	$S_{\delta V_{fl}^{RMS}}$	$S_{\delta E_\theta^{RMS}}$
"Shaping model"	0.83	0.78	0.58	0.84	0.87	0.90	0.84	0.86	0.88
"Circular model"	0.84	0.78	0.65	0.85	0.87	0.89	0.85	0.86	0.88
"2D model"	0.85	0.78	0.65	0.86	0.86	0.89	0.88	0.85	0.88

$R_{\delta A}$ and $S_{\delta A}$. The simulation results and the experimental measurements typically disagree for $\delta j_{sat}^{RMS}/\bar{j}_{sat}$ and δE_θ^{RMS}, while a better agreement is found for δV_{fl}^{RMS}, in particular for the "2D model". Concerning the accuracy of the observables, we note that $S_{\delta A} > 0.5$ for all models and plasma discharges, implying that the experimental and numerical uncertainties are rather small. Finally, as discussed in Ref. [26], we take $h_{\delta A} = 2$.

C. Probability distribution functions

To gain a deeper insight on the properties of SOL plasma turbulence, in our validation we also consider the experimental and numerical δj_{sat} and δV_{fl} PDFs, shifted such that they have the same mean and normalized to the same area, at the three locations $x - a = 0.5\,\mathrm{cm}$, $x - a = 1.2\,\mathrm{cm}$, and $x - a = 1.9\,\mathrm{cm}$. The uncertainties affecting the experimental measurements are evaluated as the standard deviation between the two δj_{sat} and δV_{fl} PDFs resulting from the probe entering and exiting the plasma. Concerning the numerical results, typical GBS simulations indicate that the numerical error affecting δj_{sat} and δV_{fl} PDFs is smaller than 0.02. The statistical error affecting the three-dimensional simulation results has similar amplitude, while for the two-dimensional simulations it is negligible. Therefore, in the following we consider the conservative values $\Delta s_{PDF(\delta j_{sat})} = \Delta s_{PDF(\delta V_{fl})} = 0.02$ and $\Delta s_{PDF(\delta j_{sat})} = \Delta s_{PDF(\delta V_{fl})} = 0.04$ for the two- and three-dimensional simulation results, respectively.

The resulting PDFs and the corresponding uncertainties are displayed in Figs. 5 and 6. We observe that, despite some small differences, in particular near the center of the distributions, the simulation results and the experimental measurements are in quite good agreement.

The agreement between simulations and experiment is confirmed by computing the values of R shown in Table VII. Indeed, at least for all three-dimensional simulations, $R < 0.2$. In

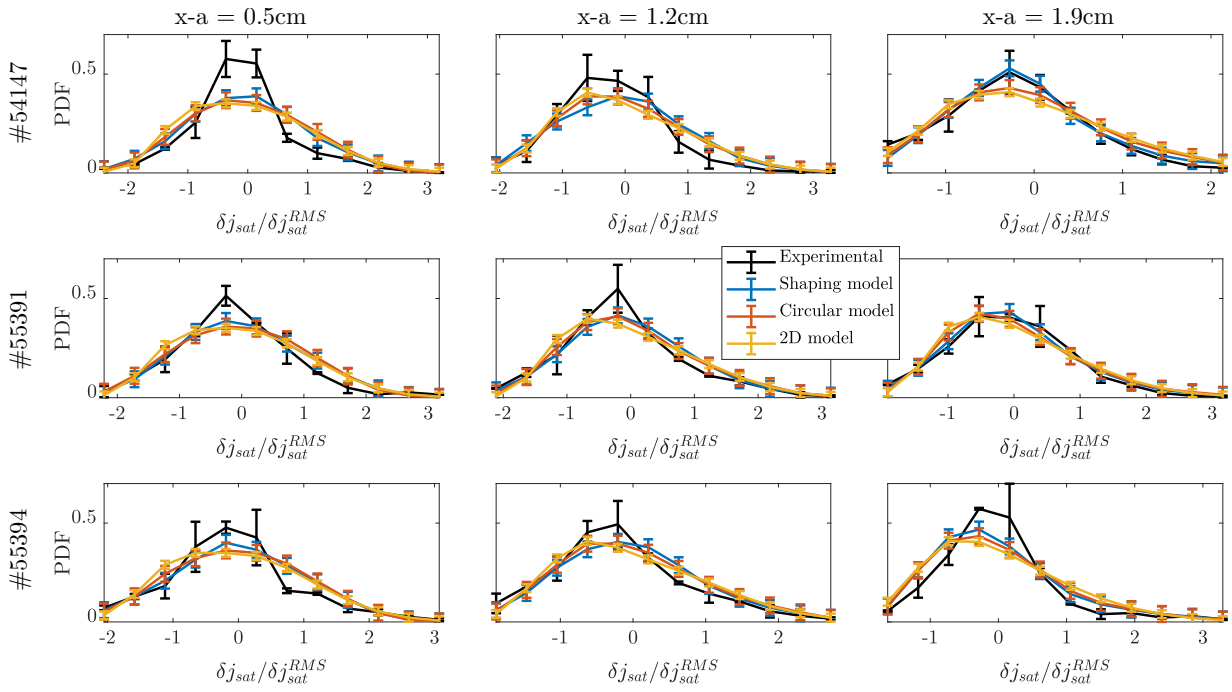

FIG. 5: PDF of δj_{sat} at the three radial positions $x-a = 0.5\,\text{cm}$, $x-a = 1.2\,\text{cm}$, and $x-a = 1.9\,\text{cm}$ for the three plasma discharges #54147, #55391, and #55394.

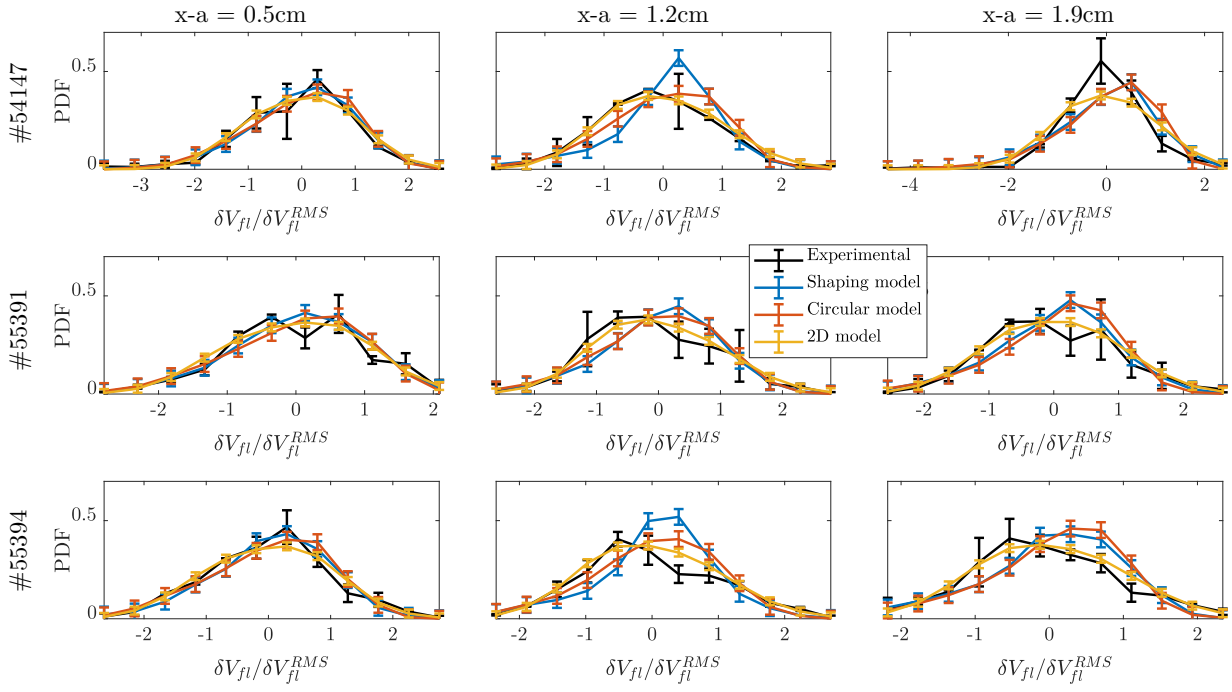

FIG. 6: PDF of δV_{fl} at the three radial positions $x-a = 0.5\,\text{cm}$, $x-a = 1.2\,\text{cm}$, and $x-a = 1.9\,\text{cm}$ for the three plasma discharges #54147, #55391, and #55394.

TABLE VII: Level of agreement between simulations and experiments with respect to the δj_{sat} and δV_{fl} PDFs.

	#54147		#55391		#55394	
	$R_{\mathrm{PDF}(\delta j_{sat})}$	$R_{\mathrm{PDF}(\delta V_{fl})}$	$R_{\mathrm{PDF}(\delta j_{sat})}$	$R_{\mathrm{PDF}(\delta V_{fl})}$	$R_{\mathrm{PDF}(\delta j_{sat})}$	$R_{\mathrm{PDF}(\delta V_{fl})}$
"Shaping model"	0.01	0.03	0.00	0.02	0.03	0.18
"Circular model"	0.03	0.02	0.00	0.04	0.06	0.08
"2D model"	0.57	0.03	0.17	0.01	0.95	0.00

TABLE VIII: Accuracy parameters for the δj_{sat} and δV_{fl} PDFs.

	#54147		#55391		#55394	
	$S_{\mathrm{PDF}(\delta j_{sat})}$	$S_{\mathrm{PDF}(\delta V_{fl})}$	$S_{\mathrm{PDF}(\delta j_{sat})}$	$S_{\mathrm{PDF}(\delta V_{fl})}$	$S_{\mathrm{PDF}(\delta j_{sat})}$	$S_{\mathrm{PDF}(\delta V_{fl})}$
"Shaping model"	0.82	0.79	0.82	0.79	0.82	0.82
"Circular model"	0.82	0.79	0.82	0.79	0.82	0.82
"2D model"	0.86	0.85	0.87	0.84	0.86	0.86

Table VIII we present the parameter S. Wee see that $0.79 < S < 0.87$, indicating that the uncertainties affecting the PDFs are small. Finally, as discussed in Ref. [26], we take $h = 2$ for the δj_{sat} and δV_{fl} PDFs.

D. Power spectral-slopes

The last two observables considered in our comparison are the j_{sat} and V_{fl} power spectral-slopes, $\alpha_{j_{sat}}$ and $\alpha_{V_{fl}}$. These are obtained by fitting the j_{sat} and V_{fl} power spectral densities (PSD) between 12 kHz and 200 kHz with a power function. More specifically, taking j_{sat} as an example, we compute the j_{sat} PSD at the three locations $x - a = 0.5$ cm, $x - a = 1.2$ cm, and $x - a = 1.9$ cm. The results are then best-fitted between $f = 12$ kHz and $f = 200$ kHz assuming $\mathrm{PSD}_{j_{sat}}(f) \propto f^{\alpha_{j_{sat}}}$. The same procedure is used to obtain $\alpha_{V_{fl}}$.

Concerning the uncertainties affecting the experimental measurements, we consider the standard deviation between the two $\alpha_{j_{sat}}$ and $\alpha_{V_{fl}}$ resulting from the probe entering and exiting the plasma, Δe^{meas}. In addition, we consider the uncertainty related to best-fitting the j_{sat}

TABLE IX: Ion saturation current and floating potential spectral-slopes and corresponding total uncertainties at $x - a = 0.5\,\mathrm{cm}$.

	#54147		#55391		#55394	
	$\alpha_{j_{sat}}$	$\alpha_{V_{fl}}$	$\alpha_{j_{sat}}$	$\alpha_{V_{fl}}$	$\alpha_{j_{sat}}$	$\alpha_{V_{fl}}$
Experimental	-2.5±0.4	-2.4± 0.5	-1.7±0.4	-1.9±0.4	-1.8±0.4	-2.2±0.4
"Shaping model"	-1.6±0.1	-1.3±0.1	-1.25±0.05	-1.2±0.1	-1.4±0.1	-1.2±0.1
"Circular model"	-1.20±0.04	-1.3±0.1	-1.3±0.1	-1.3±0.1	-1.2±0.1	-1.3±0.1
"2D model"	1.16±0.01	-1.74±0.01	-1.20±0.02	-1.76±0.03	-1.19±0.01	-1.76±0.01

TABLE X: Ion saturation current and floating potential spectral-slopes and corresponding total uncertainties at $x - a = 1.2\,\mathrm{cm}$.

	#54147		#55391		#55394	
	$\alpha_{j_{sat}}$	$\alpha_{V_{fl}}$	$\alpha_{j_{sat}}$	$\alpha_{V_{fl}}$	$\alpha_{j_{sat}}$	$\alpha_{V_{fl}}$
Experimental	-2.3±0.3	-2.3±0.6	-1.8±0.4	-2.4±0.3	-2.7±0.4	-2.7±0.4
"Shaping model"	-1.5±0.1	-1.4±0.1	-1.1±0.1	-1.1±0.1	-1.3±0.1	-1.2±0.1
"Circular model"	-1.2±0.1	-1.2±0.1	-1.3±0.1	-1.2±0.1	-1.2±0.1	-1.2±0.1
"2D model"	-1.03±0.01	-1.77±0.02	-1.07±0.02	-1.84±0.02	-1.06±0.01	-1.82±0.01

TABLE XI: Ion saturation current and floating potential spectral-slopes and corresponding total uncertainties at $x - a = 1.9\,\mathrm{cm}$.

	#54147		#55391		#55394	
	$\alpha_{j_{sat}}$	$\alpha_{V_{fl}}$	$\alpha_{j_{sat}}$	$\alpha_{V_{fl}}$	$\alpha_{j_{sat}}$	$\alpha_{V_{fl}}$
Experimental	-2.2±0.4	-1.4±1.0	-1.8±0.4	-2.6±0.6	-2.6±0.7	-2.6±0.4
"Shaping model"	-1.8±0.1	-1.9±0.1	-1.33±0.05	-1.5±0.1	-1.5±0.1	-1.7±0.1
"Circular model"	-1.4±0.1	-1.6±0.1	-1.5±0.1	-1.6±0.1	-1.5±0.1	-1.6±0.1
"2D model"	-1.19±0.02	-2.03±0.02	-1.25±0.02	-2.10±0.02	-1.18±0.01	-2.05±0.02

TABLE XII: Level of agreement between simulations and experiments with respect to the j_{sat} and V_{fl} spectral-slopes.

	#54147		#55391		#55394	
	$R_{\alpha_{j_{sat}}}$	$R_{\alpha_{V_{fl}}}$	$R_{\alpha_{j_{sat}}}$	$R_{\alpha_{V_{fl}}}$	$R_{\alpha_{j_{sat}}}$	$R_{\alpha_{V_{fl}}}$
"Shaping model"	0.89	0.53	0.23	1.00	0.98	1.00
"Circular model"	1.00	0.74	0.03	0.98	0.99	1.00
"2D model"	1.00	0.03	0.40	0.03	1.00	0.46

TABLE XIII: Accuracy parameters for the j_{sat} and V_{fl} spectral-slopes.

	#54147		#55391		#55394	
	$S_{\alpha_{j_{sat}}}$	$S_{\alpha_{V_{fl}}}$	$S_{\alpha_{j_{sat}}}$	$S_{\alpha_{V_{fl}}}$	$S_{\alpha_{j_{sat}}}$	$S_{\alpha_{V_{fl}}}$
"Shaping model"	0.89	0.81	0.86	0.87	0.86	0.88
"Circular model"	0.89	0.80	0.86	0.86	0.86	0.88
"2D model"	0.90	0.84	0.87	0.90	0.87	0.91

and V_{fl} PSDs, Δe^{fit}. This is evaluated as given by the 95% confidence interval of the best-fit of the PSDs. Finally, we assume $\Delta e^2 = (\Delta e^{fit})^2 + (\Delta e^{meas})^2$ if $\Delta e^{meas} > \Delta e^{fit}$, while we consider $\Delta e = \Delta e^{fit}$ otherwise.

Concerning the simulation results, we consider both the uncertainties related to best-fitting the PSDs with the power function, Δs^{fit}, and to the finite time-statistics, Δs^{stat}. The former are evaluated as discussed for the experimental PSDs. The latter are obtained by splitting the time traces in two sub-intervals, computing $\alpha_{j_{sat}}$ and $\alpha_{V_{fl}}$ on each sub-interval, and evaluating Δs^{fit} as the standard deviation of the two resulting values. We note that numerical and input uncertainties are neglected here since for typical GBS simulations they are smaller than Δs^{fit}.

The resulting power spectral-slopes and the corresponding total uncertainties are shown in Tables IX, X, and XI. We observe that the three-dimensional models overestimate the power spectral-slopes, while agreement within uncertainties is found for the $\alpha_{V_{fl}}$ obtained with the "2D model". This is confirmed by computing the level of agreement, as presented in

Table XII. Indeed, $R_{\alpha_{V_{fl}}} < 0.5$ for the "2D model". In Table XIII we present the parameters S. We see that $S > 0.8$, indicating that the uncertainties affecting the power spectral-slopes are small.

Finally, as discussed in Ref. [26], $h = 2$ for the j_{sat} and V_{fl} PSDs. Since the only assumption made to evaluate the power spectral-slopes from I_{sat} and V_{fl} measurements is that the PSDs are a power function of the frequency, and the uncertainty resulting from this assumption is taken into account in Δe and Δs, we use $h = 2$ also for $\alpha_{j_{sat}}$ and $\alpha_{V_{fl}}$.

V. RESULTS AND DISCUSSION

We now assess quantitatively the agreement between the three models presented in Sec. II and TCV experimental measurements by computing the metric χ and the quality factor Q. This combines the levels of agreement R, the hierarchy levels h, and the accuracy parameters S illustrated in Sec. IV. The results are presented in Table XIV.

Concerning the "Shaping model", we observe that $0.4 < \chi < 0.5$ for all the considered TCV discharges, showing that this model is able to describe equally well circular and non-circular tokamak plasma discharges. On the other hand, the agreement between experimental measurements and simulation results decreases by assuming a circular magnetic geometry in the infinite aspect ratio limit for the two negative triangularity and elongated plasma discharges #54147 and #55394, respectively. This indicates that the shaping model implemented in GBS improves the description of SOL plasma turbulence taking into account the impact of elongation and triangularity. Considering the circular discharge #55391, the "Circular model" is in slightly better agreement with the experiment than the "Shaping model". Moreover, considering the two-dimensional model, we observe that $\chi > 0.5$ for all the three plasma discharges. This indicates that the two-dimensional model considered in this study is not suitable to describe plasma turbulence in the TCV SOL. While this is a very clear results for this two-dimensional model, we speculate that a better agreement between two-dimensional simulations and experimental measurements could be obtained by considering different closures for the parallel terms (as shown for example in Refs. [33, 34]).

Since the uncertainties for all the observables are rather small (with some specific exceptions) and all the observables are at the second level of the validation hierarchy, Q is about constant in our comparison. In particular, $Q \approx 4$, which is close to the maximum value

TABLE XIV: Combined metric χ and quality factor Q, considering the ten observables discussed in Sec. IV.

	#54147		#55391		#55394	
	χ	Q	χ	Q	χ	Q
"Shaping model"	0.45	3.72	0.48	4.02	0.45	4.16
"Circular model"	0.64	3.83	0.42	4.06	0.63	4.21
"2D model"	0.59	4.11	0.56	4.33	0.75	4.43

$Q = 5$ that can be obtained by ten observables with $H = 0.5$. The Q values reported in Table XIV can be compared with the Q that would be obtained by comparing exclusively the agreement of the experimental and simulation SOL gradient scale lengths, that is $Q \leq 1.5$. Finally, we note that, to investigate the sensitivity of χ on d_0 and λ, we also computed χ for $d_0 = 0.5, 1.0, 1.5$ and $\lambda = 0.5$, and for $d_0 = 1.0$ and $\lambda = 0.1, 0.5, 1.0$. We find that, while the exact value of χ depends on d_0 and λ, the conclusions obtained in this work are not affected by varying these parameters.

The rigorous validation exercise presented herein shows that the model introduced in Ref. [28] constitutes an effective improvement of our capabilities to describe SOL turbulence in elongated magnetic equilibria with finite triangularity. This increases the reliability of our numerical results, showing that GBS simulations are a suitable tool for investigating SOL plasma turbulence in limited non-circular magnetic geometries. However, while quantities of primary importance, such as the density and temperature scale lengths, are well represented by our model, significant discrepancies persist in other observables, in particular for what concerns the level of fluctuations and the PSDs. These discrepancies can be related to, e.g., the use of a fluid model or the coupling of the SOL dynamics with the core plasma. We expect that the improvement of our model and a series of rigorous validation exercises will allow us to identify the reasons behind these discrepancies.

The present work provides a concrete example of application of the validation methodology introduced by Ricci *et al.* in Refs. [23, 24] to SOL plasma turbulence in tokamaks, showing that this methodology is able to discriminate among different models and assess the most suited to describing the experimental measurements. On the other hand, it is much more

difficult to judge a single model in absolute terms, since establishing if the observed level of agreement is acceptable or not depends on the specific purposes of the simulations.

Acknowledgments

The simulations presented herein were carried out in part at the Swiss National Supercomputing Center (CSCS) under Projects ID s655 and s718; and in part on the CINECA Marconi supercomputer within the framework of the GBSSOL and GBSedge projects. This work has been carried out within the framework of the EUROfusion Consortium and has received funding from the Euratom research and training programme 2014-2018 and 2019-2020 under grant agreement No 633053, from the RCUK Energy Programme [grant number EP/P012450/1] and from the U.S. Department of Energy under Grant No. DE-SC0010529. The views and opinions expressed herein do not necessarily reflect those of the European Commission.

---

[1] W. L. Oberkampf and T. G. Trucano. Verification and validation in computational fluid dynamics. *Progress in Aerospace Sciences* **38**, 209–272 (2002).

[2] W. L. Oberkampf and C. J. Roy. *Verification and Validation in Scientific Computing*. Cambridge University Press, New York, NY, USA (2010).

[3] P. J. Roache. *Verification and Validation in Computational Science and Engineering*. Hermosa Publishers, Albuquerque, NM, USA (1998).

[4] American Institute of Aeronautics & Astronautics. *Guide for the Verification and Validation of Computational Fluid Dynamics Simulations, G-077-1998*. American Institute of Aeronautics & Astronautics (1999).

[5] P. Roache. *Fundamentals of verification and validation*. hermosa publ. (2009).

[6] A. M. Dimits, G. Bateman, M. A. Beer, B. I. Cohen, W. Dorland, G. W. Hammett, C. Kim, J. E. Kinsey, M. Kotschenreuther, A. H. Kritz, L. L. Lao, J. Mandrekas, W. M. Nevins, S. E. Parker, A. J. Redd, D. E. Shumaker, R. Sydora, and J. Weiland. Comparisons and physics basis of tokamak transport models and turbulence simulations. *Physics of Plasmas* **7**, 969 (2000).

[7] P. Ricci, J. U. Brackbill, W. Daughton, and G. Lapenta. Collisionless magnetic reconnection in the presence of a guide field. *Physics of Plasmas* **11**, 4102 (2004).

[8] G. L. Falchetto, B. D. Scott, P. Angelino, A. Bottino, T. Dannert, V. Grandgirard, S. Janhunen, F. Jenko, S. Jolliet, A. Kendl, B. F. McMillan, V. Naulin, A. H. Nielsen, M. Ottaviani, A. G. Peeters, M. J. Pueschel, D. Reiser, T. T. Ribeiro, and M. Romanelli. The European turbulence code benchmarking effort: turbulence driven by thermal gradients in magnetically confined plasmas. *Plasma Physics and Controlled Fusion* **50**, 124015 (2008).

[9] M. M. Turner, A. Derzsi, Z. Donko, D. Eremin, S. J. Kelly, T. Lafleur, and T. Mussenbrock. Simulation benchmarks for low-pressure plasmas: Capacitive discharges. *Physics of Plasmas* **20**, 013507 (2013).

[10] R. V. Bravenec, Y. Chen, J. Candy, W. Wan, and S. Parker. A verification of the gyrokinetic microstability codes GEM, GYRO, and GS2. *Physics of Plasmas* **20**, 104506 (2013).

[11] J. Brackbill. On energy and momentum conservation in particle-in-cell plasma simulation. *Journal of Computational Physics* **317**, 405–427 (2016).

[12] F. Riva, P. Ricci, F. D. Halpern, S. Jolliet, J. Loizu, and A. Mosetto. Verification methodology for plasma simulations and application to a scrape-off layer turbulence code. *Physics of Plasmas* **21**, 062301 (2014).

[13] F. Riva, C. F. Beadle, and P. Ricci. A methodology for the rigorous verification of Particle-in-Cell simulations. *Physics of Plasmas* **24**, 055703 (2017).

[14] B. D. Dudson, J. Madsen, J. Omotani, P. Hill, L. Easy, and M. Løiten. Verification of BOUT++ by the method of manufactured solutions. *Physics of Plasmas* **23**, 062303 (2016).

[15] P. Tamain, H. Bufferand, G. Ciraolo, C. Colin, D. Galassi, P. Ghendrih, F. Schwander, and E. Serre. The TOKAM3X code for edge turbulence fluid simulations of tokamak plasmas in versatile magnetic geometries. *Journal of Computational Physics* **321**, 606–623 (2016).

[16] A. Stegmeir, D. Coster, A. Ross, O. Maj, K. Lackner, and E. Poli. GRILLIX: a 3D turbulence code based on the flux-coordinate independent approach. *Plasma Physics and Controlled Fusion* **60**, 035005 (2018).

[17] P. W. Terry, M. Greenwald, J.-N. Leboeuf, G. R. McKee, D. R. Mikkelsen, W. M. Nevins, D. E. Newman, and D. P. Stotler. Validation in fusion research: Towards guidelines and best practices. *Physics of Plasmas* **15**, 062503 (2008).

[18] M. Greenwald. Verification and validation for magnetic fusion. *Physics of Plasmas* **17**, 058101

(2010).

[19] C. Holland. Validation metrics for turbulent plasma transport. *Physics of Plasmas* **23**, 060901 (2016).

[20] S. J. Freethy, T. Görler, A. J. Creely, G. D. Conway, S. S. Denk, T. Happel, C. Koenen, P. Hennequin, A. E. White, and ASDEX Upgrade Team. Validation of gyrokinetic simulations with measurements of electron temperature fluctuations and density-temperature phase angles on ASDEX Upgrade. *Physics of Plasmas* **25**, 055903 (2018).

[21] A. E. White. Validation of nonlinear gyrokinetic transport models using turbulence measurements. *Journal of Plasma Physics* **85**, 745850101 (2019).

[22] A. Ho, J. Citrin, F. Auriemma, C. Bourdelle, F. J. Casson, H.-T. Kim, P. Manas, G. Szepesi, H. Weisen, and JET Contributors. Application of Gaussian process regression to plasma turbulent transport model validation via integrated modelling. *Nuclear Fusion* (in press).

[23] P. Ricci, C. Theiler, a. Fasoli, I. Furno, K. Gustafson, D. Iraji, and J. Loizu. Methodology for turbulence code validation: Quantification of simulation-experiment agreement and application to the TORPEX experiment. *Physics of Plasmas* **18**, 032109 (2011).

[24] P. Ricci, F. Riva, C. Theiler, A. Fasoli, I. Furno, F. D. Halpern, and J. Loizu. Approaching the investigation of plasma turbulence through a rigorous verification and validation procedure: A practical example. *Physics of Plasmas* **22**, 055704 (2015).

[25] I. Furno, F. Avino, A. Bovet, A. Diallo, A. Fasoli, K. Gustafson, D. Iraji, B. Labit, J. Loizu, S. H. Müller, G. Plyushchev, M. Podestà, F. M. Poli, P. Ricci, and C. Theiler. Plasma turbulence, suprathermal ion dynamics and code validation on the basic plasma physics device TORPEX. *Journal of Plasma Physics* **81**, 345810301 (2015).

[26] P. Ricci, C. Theiler, A. Fasoli, I. Furno, B. Labit, S. H. Muller, M. Podesta, and F. M. Poli. Langmuir probe-based observables for plasma-turbulence code validation and application to the TORPEX basic plasma physics experiment. *Physics of Plasmas* **16**, 055703 (2009).

[27] F. Hofmann, J. B. Lister, W. Anton, S. Barry, R. Behn, S. Bernel, G. Besson, F. Buhlmann, R. Chavan, M. Corboz, M. J. Dutch, B. P. Duval, D. Fasel, A. Favre, S. Franke, A. Heym, A. Hirt, C. Hollenstein, P. Isoz, B. Joye, X. Llobet, J. C. Magnin, B. Marletaz, P. Marmillod, Y. Martin, J. M. Mayor, J. M. Moret, C. Nieswand, P. J. Paris, A. Perez, Z. A. Pietrzyk, R. A. Pitts, A. Pochelon, R. Rage, O. Sauter, G. Tonetti, M. Q. Tran, F. Troyon, D. J. Ward, and H. Weisen. Creation and control of variably shaped plasmas in TCV. *Plasma Physics*

and Controlled Fusion **36**, B277–B287 (1994).

[28] F. Riva, E. Lanti, S. Jolliet, and P. Ricci. Plasma shaping effects on tokamak scrape-off layer turbulence. *Plasma Physics and Controlled Fusion* **59**, 035001 (2017).

[29] Y. Camenen, A. Pochelon, R. Behn, A. Bottino, A. Bortolon, S. Coda, A. Karpushov, O. Sauter, G. Zhuang, and the TCV team. Impact of plasma triangularity and collisionality on electron heat transport in TCV L-mode plasmas. *Nuclear Fusion* **47**, 510–516 (2007).

[30] J. Horacek, R. A. Pitts, J. Adamek, G. Arnoux, J.-G. Bak, S. Brezinsek, M. Dimitrova, R. J. Goldston, J. P. Gunn, J. Havlicek, S.-H. Hong, F. Janky, B. LaBombard, S. Marsen, G. Maddaluno, L. Nie, V. Pericoli, T. Popov, R. Panek, D. Rudakov, J. Seidl, D. S. Seo, M. Shimada, C. Silva, P. C. Stangeby, B. Viola, P. Vondracek, H. Wang, G. S. Xu, and Y. Xu. Multi-machine scaling of the main SOL parallel heat flux width in tokamak limiter plasmas. *Plasma Physics and Controlled Fusion* **58**, 074005 (2016).

[31] A. J. H. Donné. The European roadmap towards fusion electricity. *Philosophical Transactions of the Royal Society A: Mathematical, Physical and Engineering Sciences* **377**, 20170432 (2019).

[32] J. P. Graves, J. Horacek, R. A. Pitts, and K. I. Hopcraft. Self-similar density turbulence in the TCV tokamak scrape-off layer. *Plasma Physics and Controlled Fusion* **47**, L1–L9 (2005).

[33] O. E. Garcia, J. Horacek, R. A. Pitts, A. H. Nielsen, W. Fundamenski, J. P. Graves, V. Naulin, and J. J. Rasmussen. Interchange turbulence in the TCV scrape-off layer. *Plasma Physics and Controlled Fusion* **48**, L1–L10 (2006).

[34] O. Garcia, J. Horacek, R. Pitts, A. Nielsen, W. Fundamenski, V. Naulin, and J. J. Rasmussen. Fluctuations and transport in the TCV scrape-off layer. *Nuclear Fusion* **47**, 667–676 (2007).

[35] F. Nespoli, I. Furno, F. Halpern, B. Labit, J. Loizu, P. Ricci, and F. Riva. Non-linear simulations of the TCV Scrape-Off Layer. *Nuclear Materials and Energy* **0**, 1–4 (2016).

[36] C. K. Tsui, J. A. Boedo, J. R. Myra, B. Duval, B. Labit, C. Theiler, N. Vianello, W. A. J. Vijvers, H. Reimerdes, S. Coda, O. Février, J. R. Harrison, J. Horacek, B. Lipschultz, R. Maurizio, F. Nespoli, U. Sheikh, K. Verhaegh, and N. Walkden. Filamentary velocity scaling validation in the TCV tokamak. *Physics of Plasmas* **25**, 072506 (2018).

[37] S. I. Braginskii. Transport Processes in a Plasma. *Reviews of Plasma Physics* **1**, 205 (1965).

[38] A. Zeiler, J. F. Drake, and B. Rogers. Nonlinear reduced Braginskii equations with ion thermal dynamics in toroidal plasma. *Physics of Plasmas* **4**, 2134 (1997).

[39] P. Ricci, F. D. Halpern, S. Jolliet, J. Loizu, A. Mosetto, A. Fasoli, I. Furno, and C. Theiler. Simulation of plasma turbulence in scrape-off layer conditions: the GBS code, simulation results and code validation. *Plasma Physics and Controlled Fusion* **54**, 124047 (2012).

[40] F. D. Halpern, J. Horacek, R. A. Pitts, and P. Ricci. A theoretical interpretation of the main scrape-off layer heat-flux width scaling for tokamak inner-wall limited plasmas. *Plasma Physics and Controlled Fusion* **58**, 084003 (2016).

[41] J. A. Boedo, N. Crocker, L. Chousal, R. Hernandez, J. Chalfant, H. Kugel, P. Roney, and J. Wertenbaker. Fast scanning probe for the NSTX spherical tokamak. *Review of Scientific Instruments* **80**, 123506 (2009).

[42] F. Riva. *Verification and validation procedures with applications to plasma-edge turbulence simulations*. Ph.D. thesis, SB, Lausanne (2017).

[43] B. N. Rogers and P. Ricci. Low-Frequency Turbulence in a Linear Magnetized Plasma. *Physical Review Letters* **104**, 225002 (2010).

[44] P. Ricci and B. N. Rogers. Turbulence Phase Space in Simple Magnetized Toroidal Plasmas. *Physical Review Letters* **104**, 145001 (2010).

[45] P. Paruta, P. Ricci, F. Riva, C. Wersal, C. Beadle, and B. Frei. Simulation of plasma turbulence in the periphery of diverted tokamak by using the GBS code. *Physics of Plasmas* **25**, 112301 (2018).

[46] D. A. Russell, D. A. D'Ippolito, and J. R. Myra. On relaxing the Boussinesq approximation in scrape-off layer turbulence (SOLT) model simulations. *Bulletin of the American Physical Society, 54th Annual Meeting of the APS Division of Plasma Physics*, vol 57, BP8.159. Providence, Rhode Island, USA (2012).

[47] G. Q. Yu, S. I. Krasheninnikov, and P. N. Guzdar. Two-dimensional modelling of blob dynamics in tokamak edge plasmas. *Physics of Plasmas* **13**, 042508 (2006).

[48] K. Bodi, G. Ciraolo, P. Ghendrih, F. Schwander, E. Serre, and P. Tamain. Impact of the Boussinesq approximation in tokamak scrape–off layer turbulence. *38th EPS Conference on Plasma Physics*, P1.121. Strasbourg, France (2011).

[49] A. Ross, A. Stegmeir, and D. Coster. Effect of the Boussinesq approximation: Turbulence studies with GRILLIX in slab geometry. *Contributions to Plasma Physics* **58**, 478–483 (2018).

[50] J. Loizu, P. Ricci, F. D. Halpern, and S. Jolliet. Boundary conditions for plasma fluid models at the magnetic presheath entrance. *Physics of Plasmas* **19**, 122307 (2012).

[51] A. Mosetto, F. D. Halpern, S. Jolliet, J. Loizu, and P. Ricci. Finite ion temperature effects on scrape-off layer turbulence. *Physics of Plasmas* **22**, 012308 (2015).

[52] S. Coda, J. Ahn, R. Albanese, S. Alberti, E. Alessi, S. Allan, H. Anand, G. Anastassiou, Y. Andrèbe, C. Angioni, M. Ariola, M. Bernert, M. Beurskens, W. Bin, P. Blanchard, T. Blanken, J. Boedo, T. Bolzonella, F. Bouquey, F. Braunmüller, H. Bufferand, P. Buratti, G. Calabró, Y. Camenen, D. Carnevale, F. Carpanese, F. Causa, R. Cesario, I. Chapman, O. Chellai, D. Choi, C. Cianfarani, G. Ciraolo, J. Citrin, S. Costea, F. Crisanti, N. Cruz, A. Czarnecka, J. Decker, G. De Masi, G. De Tommasi, D. Douai, M. Dunne, B. Duval, T. Eich, S. Elmore, B. Esposito, M. Faitsch, A. Fasoli, N. Fedorczak, F. Felici, O. Février, O. Ficker, S. Fietz, M. Fontana, L. Frassinetti, I. Furno, S. Galeani, A. Gallo, C. Galperti, S. Garavaglia, I. Garrido, B. Geiger, E. Giovannozzi, M. Gobbin, T. Goodman, G. Gorini, M. Gospodarczyk, G. Granucci, J. Graves, R. Guirlet, A. Hakola, C. Ham, J. Harrison, J. Hawke, P. Hennequin, B. Hnat, D. Hogeweij, J.-P. Hogge, C. Honoré, C. Hopf, J. Horáček, Z. Huang, V. Igochine, P. Innocente, C. Ionita Schrittwieser, H. Isliker, R. Jacquier, A. Jardin, J. Kamleitner, A. Karpushov, D. Keeling, N. Kirneva, M. Kong, M. Koubiti, J. Kovacic, A. Krämer-Flecken, N. Krawczyk, O. Kudlacek, B. Labit, E. Lazzaro, H. Le, B. Lipschultz, X. Llobet, B. Lomanowski, V. Loschiavo, T. Lunt, P. Maget, E. Maljaars, A. Malygin, M. Maraschek, C. Marini, P. Martin, Y. Martin, S. Mastrostefano, R. Maurizio, M. Mavridis, D. Mazon, R. McAdams, R. McDermott, A. Merle, H. Meyer, F. Militello, I. Miron, P. Molina Cabrera, J.-M. Moret, A. Moro, D. Moulton, V. Naulin, F. Nespoli, A. Nielsen, M. Nocente, R. Nouailletas, S. Nowak, T. Odstrčil, G. Papp, R. Papřok, A. Pau, G. Pautasso, V. Pericoli Ridolfini, P. Piovesan, C. Piron, T. Pisokas, L. Porte, M. Preynas, G. Ramogida, C. Rapson, J. Juul Rasmussen, M. Reich, H. Reimerdes, C. Reux, P. Ricci, D. Rittich, F. Riva, T. Robinson, S. Saarelma, F. Saint-Laurent, O. Sauter, R. Scannell, C. Schlatter, B. Schneider, P. Schneider, R. Schrittwieser, F. Sciortino, M. Sertoli, U. Sheikh, B. Sieglin, M. Silva, J. Sinha, C. Sozzi, M. Spolaore, T. Stange, T. Stoltzfus-Dueck, P. Tamain, A. Teplukhina, D. Testa, C. Theiler, A. Thornton, L. Tophøj, M. Tran, C. Tsironis, C. Tsui, A. Uccello, S. Vartanian, G. Verdoolaege, K. Verhaegh, L. Vermare, N. Vianello, W. Vijvers, L. Vlahos, N. Vu, N. Walkden, T. Wauters, H. Weisen, M. Wischmeier, P. Zestanakis, and M. Zuin. Overview of the TCV tokamak program: scientific progress and facility upgrades. *Nuclear Fusion* **57**, 102011 (2017).

[53] J.-M. Moret, B. Duval, H. Le, S. Coda, F. Felici, and H. Reimerdes. Tokamak equilibrium reconstruction code LIUQE and its real time implementation. *Fusion Engineering and Design* **91**, 1–15 (2015).

[54] C. K. Tsui, J. A. Boedo, F. D. Halpern, J. Loizu, F. Nespoli, J. Horacek, B. Labit, J. Morales, H. Reimerdes, P. Ricci, C. Theiler, S. Coda, B. P. Duval, and I. Furno. Poloidal asymmetry in the narrow heat flux feature in the TCV scrape-off layer. *Physics of Plasmas* **24**, 062508 (2017).

[55] C. K. Tsui, J. A. Boedo, and P. C. Stangeby. Accounting for Debye sheath expansion for proud Langmuir probes in magnetic confinement fusion plasmas. *Review of Scientific Instruments* **89**, 013505 (2018).

[56] F. Halpern and P. Ricci. Velocity shear, turbulent saturation, and steep plasma gradients in the scrape-off layer of inner-wall limited tokamaks. *Nuclear Fusion* **57**, 034001 (2017).

[57] F. Nespoli, B. Labit, I. Furno, J. Horacek, C. Tsui, J. Boedo, R. Maurizio, H. Reimerdes, C. Theiler, P. Ricci, F. Halpern, U. Sheikh, K. Verhaegh, R. Pitts, and F. Militello. Understanding and suppressing the near scrape-off layer heat flux feature in inboard-limited plasmas in TCV. *Nuclear Fusion* **57**, 126029 (2017).

[58] F. Riva, L. Milanese, and P. Ricci. Uncertainty propagation by using spectral methods: A practical application to a two-dimensional turbulence fluid model. *Physics of Plasmas* **24**, 102302 (2017).

[59] F. Riva, N. Vianello, M. Spolaore, P. Ricci, R. Cavazzana, L. Marrelli, and S. Spagnolo. Three-dimensional simulations of plasma turbulence in the RFX-mod scrape-off layer and comparison with experimental measurements. *Physics of Plasmas* **25**, 022305 (2018).